

# Reconfigurable Training, Vortex Writing and Spin-Wave Fingerprinting in an Artificial Spin-Vortex Ice

Jack Gartside (✉ [j.carter-gartside13@imperial.ac.uk](mailto:j.carter-gartside13@imperial.ac.uk))

Imperial College London <https://orcid.org/0000-0002-7044-7399>

Kilian Stenning

Imperial College London

Alex Vanstone

Imperial College London

Troy Dion

Imperial College London

Holly Holder

Imperial College London

Daan Arroo

Imperial College London

Hidekazu Kurebayashi

UCL <https://orcid.org/0000-0002-2021-1556>

Will Branford

Imperial College London <https://orcid.org/0000-0002-4821-4097>

---

## Article

**Keywords:** artificial spin systems, vortex writing, spin-wave fingerprinting

**Posted Date:** July 22nd, 2021

**DOI:** <https://doi.org/10.21203/rs.3.rs-736619/v1>

**License:**  This work is licensed under a Creative Commons Attribution 4.0 International License.

[Read Full License](#)

---

**Version of Record:** A version of this preprint was published at Nature Nanotechnology on May 5th, 2022.  
See the published version at <https://doi.org/10.1038/s41565-022-01091-7>.

# Reconfigurable Training, Vortex Writing and Spin-Wave Fingerprinting in an Artificial Spin-Vortex Ice

Jack C. Gartside<sup>1,†,\*</sup>, Kilian D. Stenning<sup>1,†</sup>, Alex Vanstone<sup>1,†</sup>, Troy Dion<sup>1,2</sup>, Holly H. Holder<sup>1</sup>, Daan M. Arroo<sup>1,2</sup>, Hidekazu Kurebayashi<sup>2</sup>, and Will R. Branford<sup>1,3</sup>

<sup>1</sup>Blackett Laboratory, Imperial College London, London SW7 2AZ, United Kingdom

<sup>2</sup>London Centre for Nanotechnology, University College London, London WC1H 0AH, United Kingdom

<sup>3</sup>London Centre for Nanotechnology, Imperial College London, London SW7 2AZ, United Kingdom

†These authors contributed equally

\*Corresponding author e-mail: j.carter-gartside13@imperial.ac.uk

## ABSTRACT

Strongly-interacting artificial spin systems are moving beyond mimicking naturally-occurring materials to find roles as versatile functional platforms, from reconfigurable magnonics to designer magnetic metamaterials. Typically artificial spin systems comprise nanomagnets with a single magnetisation texture: collinear macrospins or chiral vortices.

By tuning nanoarray dimensions we achieve macrospin/vortex bistability and demonstrate a four-state metamaterial spin-system ‘Artificial Spin-Vortex Ice’ (ASVI). ASVI is capable of adopting Ising-like macrospins with strong ice-like vertex interactions, in addition to weakly-coupled vortices with low stray dipolar-field.

The enhanced bi-texture microstate space gives rise to emergent physical memory phenomena, with ratchet-like vortex training and history-dependent nonlinear training dynamics. We observe vortex-domain formation alongside MFM tip vortex-writing. Tip-written vortices dramatically alter local reversal and memory dynamics.

Vortices and macrospins exhibit starkly-differing spin-wave spectra with analogue-style mode-amplitude control via vortex-training and mode-frequency shifts of  $\Delta f = 3.8$  GHz. We leverage spin-wave ‘spectral fingerprinting’ for rapid, scaleable readout of vortex and macrospin populations over complex training-protocols with applicability for functional magnonics and physical memory.

## Introduction

Artificial spin systems<sup>1</sup> are metamaterials representing magnetic spins via the magnetisation textures of nanomagnetic elements. Typically a single magnetisation texture is employed across the system, i.e. Ising-like macrospins in nanoislands<sup>2</sup> or vortex-states in nanodisks<sup>3</sup> with nanoelement dimensions tuned to energetically favour that texture throughout the array. These simple systems have enabled fascinating science and observation of diverse phenomena including emergent ‘magnetic-monopole’ defects<sup>4</sup> and spontaneous long-range ordering<sup>5</sup>. However, limiting systems to single textures places arbitrary constraints on the complexity of emergent behaviours. The great freedom of artificial spin systems & metamaterials at large is that properties may be tailored through nanofabrication, allowing complex ‘designer’ behaviours not observed in nature. Recently four-state systems were presented using pairs of Ising-like macrospins to represent ‘metaspins’<sup>6</sup> or square nanomagnets with four-state Potts behaviour<sup>7</sup> with enhanced microstate-spaces and corresponding emergent behaviours not observed in two-state Ising or vortex systems. These systems still employ single magnetisation textures, with much promised by expanding the texture range.

Reconfigurable magnonics<sup>8–11</sup>, physical memory<sup>12</sup> and hardware neuromorphic computation<sup>13–15</sup> are critical future technologies reliant on rich, diverse microstate-spaces to fulfill their promise. To meet this need we present an approach embracing metamaterial engineering and bypassing single-texture limitations. By tailoring nanoelements such that Ising and vortex states are equally energetically-favourable we present artificial spin vortex ice (ASVI) - a four-state, bi-texture spin-system; two Ising-like macrospin orientations and two vortex chiralities. We define ASVI as a strongly-interacting nanomagnetic array with Ising-like macrospins where interactions favour ice-rule configurations, and vortices exhibiting flux-closure patterns with low stray dipolar-field.

The bistable texture drives emergent physical-memory properties. Vortices are stable to higher field than macrospins, allowing ratchet-like vortex-training intriguingly analogous to low-temperature Skyrmion field-training<sup>16</sup>. Low vortex stray-field disrupts the dipolar field landscape, pinning or promoting reversal of adjacent bars. This is leveraged for targeted local

control of memory and switching dynamics via MFM-tip writing of vortices and complex nonlinear training protocols. The array incorporates thinner bars tuned for macrospin-stability providing a reconfigurable bias-field exerting control over training dynamics.

Magnons are highly-sensitive to magnetic texture<sup>17</sup> and the bistable ASVI textures expand horizons of reconfigurable magnonics, with  $\Delta f = 3.8$  GHz between vortex and macrospin modes and highly-nonlinear vortex-mode field-gradients. We demonstrate fine analogue-style tuning of mode amplitudes via vortex-training, affording exceptional levels of spectral control and reconfigurability relative to existing reconfigurable magnonic crystals. We leverage the spectral-response for ‘spin-wave fingerprinting’<sup>18</sup> vortex/macropin population readout and rapid, scaleable measurement of physical memory effects.

## Results and Discussion

### Artificial spin-vortex ice

The ASVI studied here is based on square lattice ASI<sup>5</sup>, with alternating rows of thin and wide bars along  $\hat{x}$  (fig. 1 a). Different coercive fields for thin and wide bars permit global-field microstate control as described previously<sup>19</sup>. Bars are permalloy, 600 nm long, 200 nm (wide-bar) and 125 nm (thin-bar) wide and 20 nm thick with 100 nm vertex gap (bar-end to vertex-centre). Along  $\hat{x}$ , wide-bar coercive field distribution is  $H_{c1} = 15.5 - 17$  mT, thin bar coercive field  $H_{c2} = 26 - 29$  mT. Wide-bar dimensions are chosen such that the combined demagnetisation and exchange energy of the macrospin state are equal to the vortex state (via MuMax3 simulation, fig. 1 b), giving macrospin and vortex bistability<sup>20-22</sup>. The ASVI considered here is bicomponent, with macrospin/vortex transition occurring in wide bars. Thin bars remain in macrospin states to provide a reconfigurable dipolar bias-field landscape. Figure 1 c,d show MuMax3 magnetisation simulations of a single ASVI vertex in all-macrospin (c) and wide-bar vortex, thin-bar macrospin (d) states with corresponding simulated magnetic force microscope (MFM) images e,f. Vertex gap is exaggerated relative to the experimental sample to allow clearer visualisation. Vortex bars exhibit a characteristic ‘checkered’ pattern under MFM, with diagonally-opposite quadrants of positive (white) and negative (dark) magnetic charge. Vortex chirality readout is possible via the relative orientations of dark and light quadrants. Fig. 1 g,h show experimental MFM images of all-macrospin (g) and a vortex chain in an otherwise macrospin state (h). Vortices are slightly distorted in the experimental MFM image relative to simulation, due in part to tip-sample interactions favouring attractive (dark) over repulsive (light) interaction<sup>23</sup>. Figure 1 i shows an MFM image of ASVI after 30 training field loops at  $\pm 18$  mT ( $\pm$  denotes bipolar loop applying +18 mT then -18 mT), exhibiting a mixed macrospin/vortex state with several vortex chains and both vortex chiralities observed.

Figure 1 j) shows a simulated MuMax3 time series of the vorticisation process. An initial  $-\hat{x}$  saturated vertex ( $t=0$ ) is field-swept along  $+\hat{x}$  with a  $1^\circ$  angular-offset such that the bottom-right wide-bar experiences slightly higher field-torque and switches first.  $\mathbf{H}_{ext}$  brings the topological charge  $Q_T = +\frac{1}{2}$  edge-bound topological defects at either bar-end to opposite long-edges ( $t=0.4$  ns), creating pockets of  $+\hat{x}$  magnetisation (red regions) which spread through the bar ( $t=0.58$  ns). In normal macrospin reversal, the  $\mathbf{M} = +\hat{x}$  region growth continues and the  $Q_T = +\frac{1}{2}$  defects finish at opposite bar ends. However, in vorticisation one of the  $Q_T = +\frac{1}{2}$  defects reverses direction halfway ( $t=0.78$  ns). This is the crucial step differentiating macrospin-to-macrospin reversal from macrospin-to-vortex conversion. The defects now come into close proximity at the vertex-centre bar end ( $t=1$  ns) before combining into a single  $Q_T = +1$ -defect ( $t=1.25$  ns). Integer-charge defects may only exist in the magnet bulk, and a  $Q_T = +1$ -defect is otherwise known as a vortex-core. The vortex-core moves into the nanomagnet bulk ( $t=1.75$  ns) before reaching a central equilibrium point, minimising exchange and demagnetisation energy ( $t=2.43$  ns). The factors causing one  $Q_T = +\frac{1}{2}$  defect to reverse direction and drive vorticisation may be isolated in simulation, but are more stochastic in experiment. Angularly offsetting  $H_{app}$  from  $\hat{x}$  or  $\hat{y}$  encourages vorticisation in simulation by generating unequal field torques on the  $Q_T = +\frac{1}{2}$  defects at either macrospin end. This effect was not observed in experiment, possibly due to edge-roughness affecting edge-defect trajectories and stochastic room-temperature thermal effects versus effective 0 K simulation. Simulation and experiment both find vorticisation more common when beginning from a type-1 microstate due to unbalanced dipolar fields from opposingly-magnetised thin and wide bars generating unequal field-torque on the two  $Q_T = +\frac{1}{2}$  defects.

To study how vorticisation progresses throughout training, figure 1 k) shows MFM image-series where an all-macrospin,  $-\hat{x}$ -saturated ASVI (top-left panel) is subjected to four sequential  $\pm 18$  mT  $\hat{x}$  training loops and imaged after each field. 18 mT is chosen such that thin bars never reverse while wide bars reverse each field application, save for those becoming pinned via local microstate-dependent dipolar-field textures (i.e. left and top edges of 3-loop, negative field panel). 18 mT is below the vortex-to-macrospin (V2M) conversion field (20 mT for the relative  $\mathbf{H}_{ext}$  & array orientation here), creating a ratchet effect where some macrospins are vorticised each loop but not vice-versa, increasing vortex population throughout training. V2M conversion is examined further in figure 4.

Vortices initially appear with stochastic placement (fig. 1k - 0 loops, +ve field). As training progresses, vorticisation occurs preferentially adjacent to existing vortices. This is due to the low dipolar field emanating from vortex bars causing asymmetry

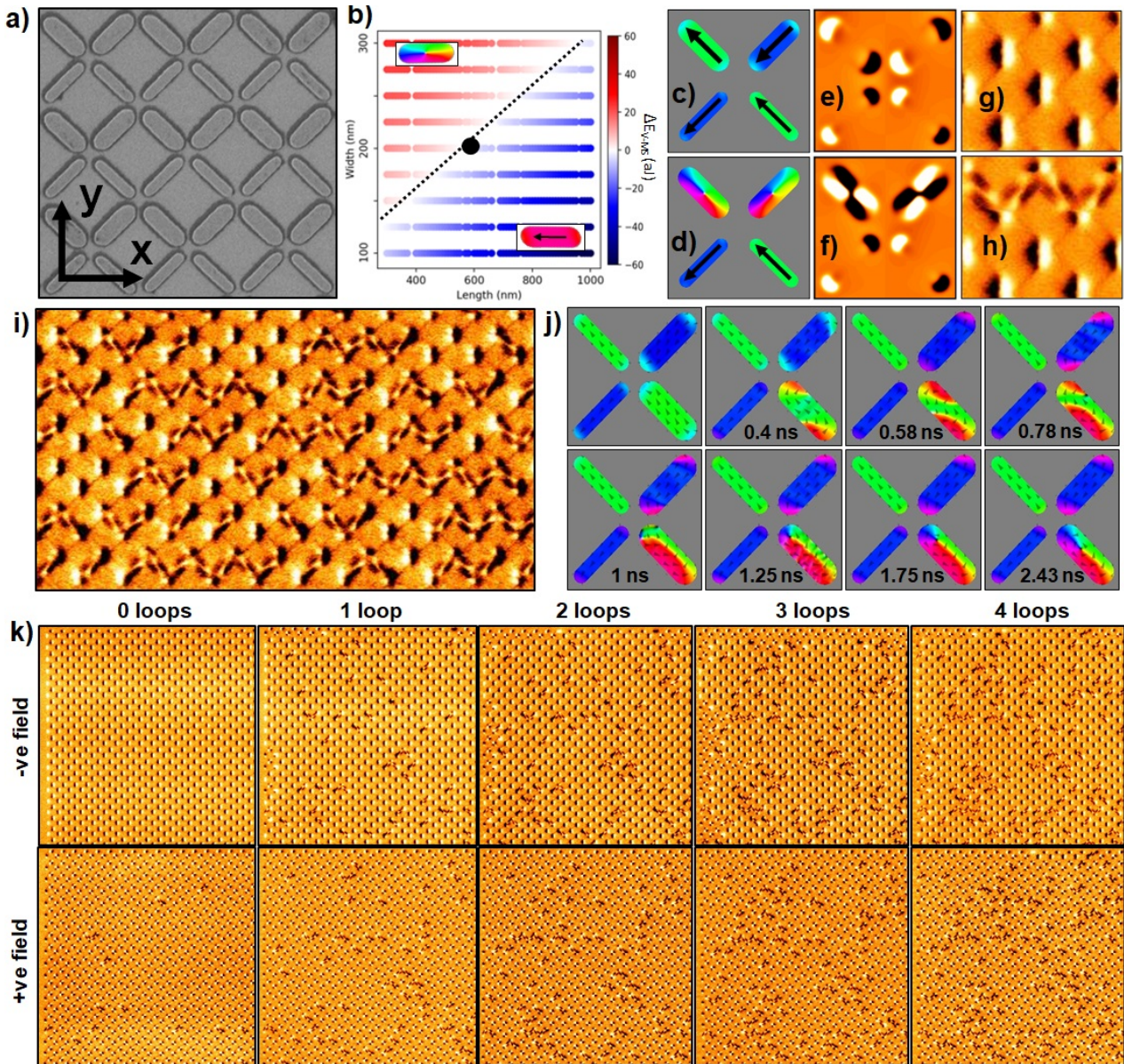


**Figure 1.** Artificial spin-vortex ice.

a) Scanning electron micrograph of artificial spin-vortex ice. Permalloy bars are 600 nm long, 200 nm (wide-bar) and 125 nm (thin-bar) wide, 20 nm thick with 100 nm vertex gap (bar-end to vertex-centre). Lattice vectors  $\hat{x}$  (along wide/thin bar rows) and  $\hat{y}$  (perpendicular to rows) are defined.

b) Phase diagram of energy-difference between vortex and macrospin states for a range of bar dimensions, determined via MuMax3 simulation. Red regions favour vortex states, blue favour macrospin. Dotted black line indicates dimensions with equal macrospin and vortex energy, black circle at 600 nm X 200 nm indicates wide-bar dimensions of sample studied here.

c,d) MuMax3-simulated magnetisation states of a single 4-bar vertex in all-macrospin (c) and wide-bar vortex, thin-bar macrospin (d) states. e,f) Simulated MFM images produced from magnetisation states (c,d), corresponding to (e,f) respectively. Images simulated for 60 nm tip height above sample.

g,h) Experimental magnetic force microscope images of all-macropin (g) and mixed vortex-macropin (h) states.

i) Magnetic force microscope image ( $12 \times 6 \mu\text{m}^2$ ) of mixed vortex-macropin state. State is prepared by 30 training loops at  $\pm 18 \text{ mT}$ , beginning from a -200 mT saturated pure-macropin state. Wide bars are observed in both macropin and vortex states, thin bars all remain macropin.

j) MuMax3 time-series of vortication process at  $H_{app} = 16 \text{ mT}$ . Macropin state in bottom right bar changes to a vortex via topological-defect exchange combining two half-integer, edge bound defects from opposite bar ends in the macropin state into a single +1 winding number topological vortex-core defect in the bulk of the nanomagnet.

k) Magnetic force micrograph series ( $15 \times 15 \mu\text{m}^2$  images) showing four-loop vortex-training sequence from initial  $-\hat{x}$  saturated, pure-macropin state (0 loop, -ve field). Training field amplitude is 18 mT, applied along  $\hat{x}$ . Series continues for 5, 7 and 10 loops, shown in supplementary figure 1. Formation of vortex and macropin domains is observed as training progresses to higher loop numbers. All images taken in zero-field.

in the local dipolar-field texture and increasing likelihood of asymmetric field-torque on  $Q_T = +\frac{1}{2}$  defects during switching. This local promotion of vorticisation leads to formation of vortex and macrospin domains, with defined domain-structures taking shape by the 4 loop, +ve field image and clearly observed as training continues to 5-10 loops (supplementary figure 1) and in higher loop-number images in fig. 2 g). A higher vorticisation probability is observed when moving from positive to negative field, 3.05% macrospins vorticising per loop vs. 1.34% when switching from negative to positive. As mentioned above this is due to different microstates and dipolar-field landscapes between field polarities. Thin bars remain magnetised along  $-\hat{x}$  while wide bars reverse, hence negative fields place macrospins in ‘type 2’ spin-ice states<sup>19</sup> (0 loop, -ve field panel) while positive fields give ‘type 1’ or ground-states<sup>5,24,25</sup> (macrospins in 0 loop, +ve field panel). The two states have differing dipolar-field landscapes, in type 2 wide and thin bars are magnetised the same way, giving symmetric dipolar field at the vertex, while type 1 has oppositely-magnetised wide and thin bars which gives an unbalanced dipolar-field texture due to the stronger dipolar-field of the wide bar. Again this is more likely to give unbalanced field-torques on  $Q_T = +\frac{1}{2}$  defects, driving them to combine to a  $Q_T = +1$  vortex state.

To demonstrate vorticisation stochasticity, we compare three separate training sequences each beginning from saturated all-macrospin states. Figure 1 k), fig. 2 g) and supplementary figure 1 show different vortex locations and domain structures forming on the same array area, confirming vorticisation is a stochastically-dominated process, rather than determined by nanofabrication-imperfections termed ‘quenched disorder’ favouring spatially-similar domain patterns each training sequence.

### Reconfigurable-directed vortex training and spin-wave signatures

We have observed via MFM with single-bar resolution how vorticisation occurs. MFM is an intrinsically slow process, each image takes 10-30 minutes with scan-windows limited  $\sim 10 - 100 \mu\text{m}$ . It requires cumbersome mechanical apparatus, unsuitable for device integration. Ferromagnetic resonance (FMR) has emerged as a rapid, scaleable on-chip microstate readout technique well-suited to strongly-interacting nanomagnetic arrays<sup>18</sup>. While not providing single-spin, exact microstate resolution, FMR can elucidate fine microstate details including ASI vertex-type populations and domain sizes<sup>18</sup>, unavailable via magnetometry such as MOKE or VSM. Here we employ FMR to spectrally fingerprint vortex-trained states.

We analyse mode frequencies following the Kittel equation<sup>26</sup>  $f = \frac{\mu_0 \gamma}{2\pi} \sqrt{\mathbf{H}(\mathbf{H} + \mathbf{M})}$  in the  $k=0$  limit applicable to this work,  $\gamma$  is the gyromagnetic ratio and  $\mathbf{H} = \mathbf{H}_{ext} + \mathbf{H}_{loc}$ , the globally-applied field  $\mathbf{H}_{ext}$  and the local dipolar-field of the nanomagnets  $\mathbf{H}_{loc}$ . The local dipolar-field landscape varies greatly as training and vorticisation progress, with resulting distinct microstate-dependent magnon spectra. To focus on the effects of training on the microstate and vortex population, spectra are measured at a consistent small bias-field, chosen for good vortex-mode signal-to-noise. All spectral differences may therefore be attributed to microstate changes and corresponding shifts in  $\mathbf{H}_{loc}$ <sup>18</sup>. Broadband FMR spectra were measured in differential  $\frac{\partial P}{\partial \mathbf{H}}$  mode, 10 MHz frequency resolution with samples excited by mm-scale coplanar waveguide.

Figure 2 a) shows differential FMR spectra measured after the negative-field arm of each  $\pm 18 \text{ mT}$  loop over a 30 loop training sequence. Initial 0-loop state (dark blue trace) is  $-\hat{x}$  saturated, all-macrospin state, training field is then applied along  $\hat{x}$ . Colour-scale denotes training-loop number, final 30-loop state is dark-red. The initial all-macrospin state exhibits two modes, a wide-bar macrospin mode at 7 GHz and thin-bar macrospin mode at 8.8 GHz. As training progresses, the wide-bar mode decreases in amplitude as vortex-training converts macrospins to vortices. Wide-bar macrospin mode-frequency redshifts throughout training as  $\mathbf{H}_{loc}$  is reduced by increasing numbers of flux-closed vortices, shifting 0.4 GHz after 30 loops. Similarly the thin-bar mode is blueshifted 0.15 GHz. As the wide-bar macrospin mode decreases, a new 3.5 GHz vortex-mode grows with equal vortex and macrospin mode amplitudes by 10 loops and vortex-mode amplitude double the macrospin at 30 loops. Fine shifts in mode amplitude and frequency are observed throughout training, demonstrating the capability of vortex-training to tailor relative mode power and frequency and provide on-demand spectral reconfiguration with more subtle, analogue-style control available than via reconfiguration of entire microstates<sup>19</sup>. The correspondence of mode-amplitude to vortex and macrospin populations demonstrates the applicability of ‘spin-wave fingerprinting’ to multi-texture spin-systems<sup>18</sup>.

So far we have considered thin-bars as providing a static dipolar bias-field. We may exploit their magnetisation states as an extra degree of freedom and reconfigurably ‘direct’ vortex training. Figure 2 b) shows peak-amplitude extractions of wide-bar macrospin and vortex modes over 30-loop training sequences for three distinct cases: wide-bars and thin-bars initially saturated along  $-\hat{x}$  as in fig. 2 a) (blue and orange traces), wide-bars saturated along  $-\hat{x}$ , thin-bars along  $+\hat{y}$  (green and red traces), and wide and thin bars saturated along  $+\hat{y}$  (brown and purple traces). Training field is applied along wide-bar saturation axis in each case. Macrospin mode amplitude is fitted with  $y = Ae^{-\tau_{MS}x} + c$ , with decay constant  $\tau_{MS}$  the macrospin training rate and  $c$  corresponding to the final macrospin population. Vortex mode amplitude is fitted as  $y = k - Be^{-\tau_V x}$  with  $\tau_V$  the vortex training rate &  $k$  relating to final vortex population. For all cases, distinct training rates and final vortex/macrospin populations are observed - showing the degree of control available from the thin bars and the sensitivity of vorticisation to dipolar-field texture. We may tailor training behaviour via the reconfigurable bias-field from the thin bars, and while spatially uniform thin-bar states are prepared here one may locally define arbitrary thin-bar magnetisation states<sup>27,28</sup> to spatially texture training.

Exploring vortex-mode field evolution, figure 2 c-f) shows FMR heatmaps for 0-30 training-loop states. For the 0-loop,

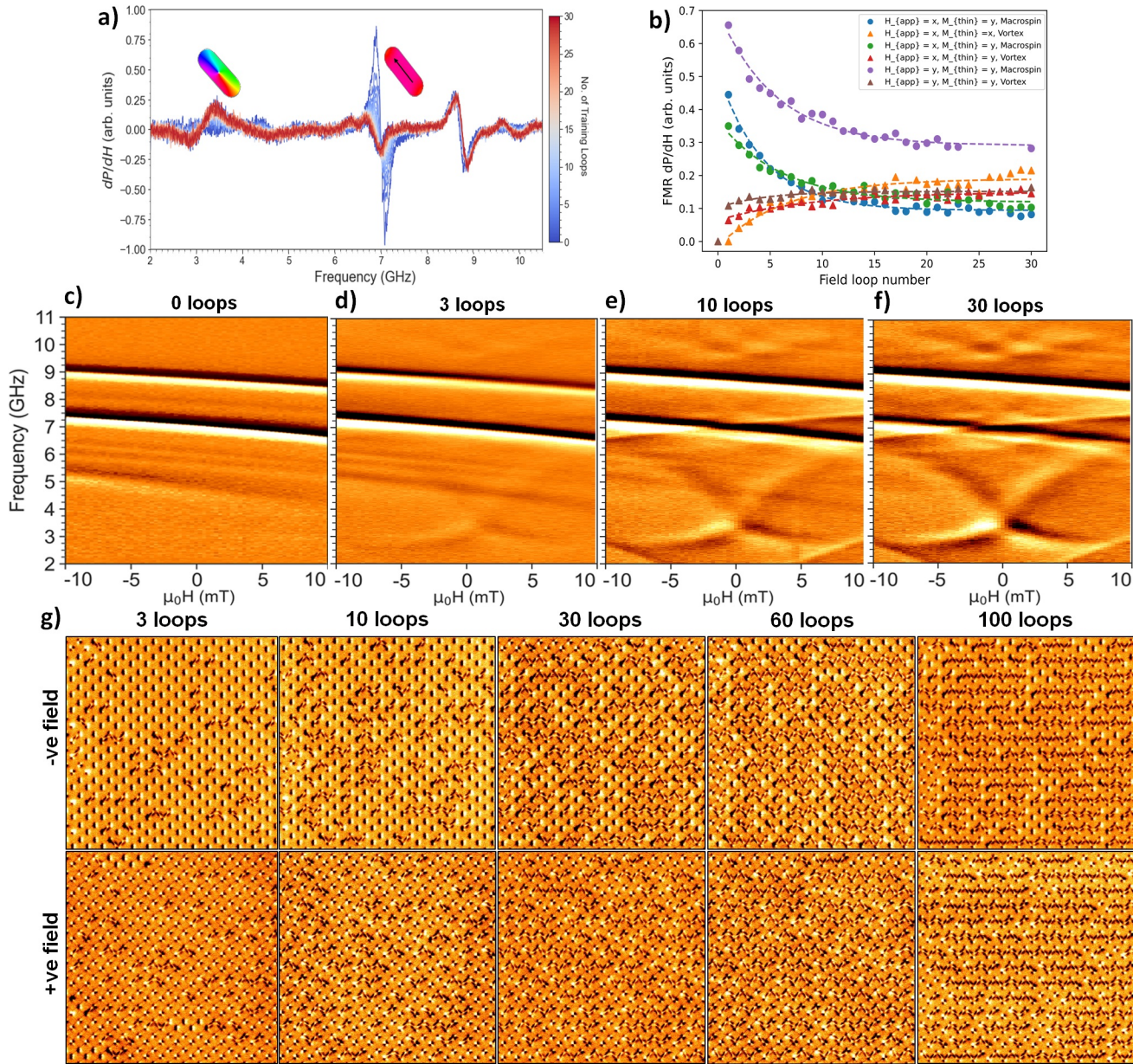


**Figure 2.** Reconfigurable-directed vortex training and spin-wave spectra.

a) Differential FMR spectra measured in  $-1.2$  mT bias field after  $0\text{-}30$  successive  $\pm 18$  mT training loops. Zero-loop state corresponds to  $-200$  mT saturated pure-macrospin state. Four main modes are observed: low-frequency vortex mode ( $\sim 3.5$  GHz), wide-bar macrospin mode ( $\sim 7$  GHz), thin-bar macrospin mode ( $\sim 8.8$  GHz) and high-frequency vortex mode ( $\sim 9.75$  GHz).

b) Mode-amplitude of low-frequency vortex and wide-bar macrospin modes for  $0\text{-}30 \pm 18$  mT training loops. Curves are displayed for three cases: 1 - Training-field along  $\hat{x}$  orientation,  $-\hat{x}$  saturated thin-bars (blue, orange points). 2 - Training-field along  $\hat{x}$  orientation,  $+\hat{y}$  saturated thin-bars (green, red points). 3 - Training-field along  $\hat{y}$  orientation,  $+\hat{y}$  saturated thin-bars (purple, brown points). Dashed lines for macrospin modes are exponential decay fits  $y = Ae^{-\tau_{MS}x} + c$ , with decay constant  $\tau$  the training rate and  $c$  corresponding to the final macrospin population, vortex modes fits are  $y = k - e^{-\tau_{VX}x}$ . Different training rates and final vortex/macrospin populations are observed for the three cases, demonstrating reconfigurable-directed training via thin-bar dipolar bias-field landscape and training-field  $\hat{x}/\hat{y}$  orientation relative to the sample lattice.

c-f) Differential  $\pm 10$  mT FMR heatmaps measured after  $0$  (c),  $3$  (d),  $10$  (e) and  $30$  (f)  $\pm 18$  mT training loops. Sample was initially saturated along  $-\hat{x}$ , training field applied along  $\hat{x}$ .  $\chi$ -shaped low-frequency vortex mode and ‘checkerboard’ high-frequency vortex modes increase with intensity throughout training.

g) MFM series of  $3\text{-}100 \pm 18$  mT training-loop states imaged after negative (top row) and positive (bottom row) fields of each training-loop. Increasing numbers of vortex-state bars are observed as training progresses, matching the increasing vortex FMR-mode intensity in c-f) heatmaps. Images are  $15 \mu\text{m}$  square.

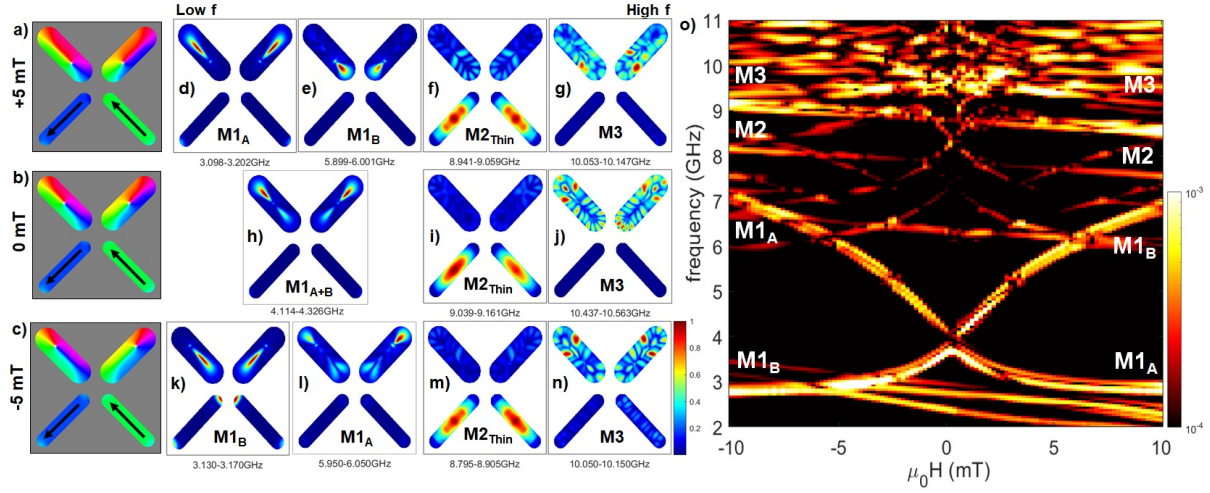


**Figure 3.** Simulated spatial magnon mode-power maps and heatmap.

a-c) MuMax3 magnetisation states of ASVI vertex with both wide bars in vortex state at  $H_{app}=+5$  mT (a), 0 mT (b) and -5 mT (c). Vortex core is displaced along bar length by  $H_{app}$ , leading to two low-frequency 3-6 GHz modes corresponding to magnetisation regions above ( $M1_A$ ) and below ( $M1_B$ ) the vortex core. Both vortices here are the same chirality,  $M1_A$  and  $M1_B$  are inverted in terms of high/low frequency at a given field for opposite chirality vortices.

d-n) Spatial magnon mode power maps for the  $M1_A$  and  $M1_B$  vortex modes,  $M2$  thin-bar macrospin mode and  $M3$  whispering-gallery like vortex mode.

o) Simulated heatmap showing mode-dispersion with field.

all-macrospin state wide-bar ( $\sim 7$  GHz) and thin-bar ( $\sim 9$  GHz) nanobar-centre localised modes are observed, alongside a higher-index thin-bar mode ( $\sim 8$  GHz) and three higher-index wide-bar macrospin modes ( $\sim 5, 6, 6.5$  GHz). After 3 training loops, new mode structures are observed with a pair of sigmoid-like modes between  $2.5 - 6.5$  GHz forming an  $\chi$ -shaped structure intersecting at  $+1$  mT. These striking new modes correspond to the vortex state, increasing in amplitude in the 10-loop heatmap as more bars vorticise. Checkerboard-pattern higher-index 9.5-10.5 GHz vortex modes with near-zero field-gradient also become visible at 10 loops. The 10-loop heatmap shows a lower-amplitude wide-bar macrospin mode with opposite (negative) gradient, corresponding to the population of oppositely magnetised wide bars, pinned by  $\mathbf{H}_{loc}$  as observed in higher loop-number MFM images. Vortex modes continue to increase in amplitude in the 30-loop heatmap, as does the oppositely-magnetised wide-bar macrospin mode. The opposing wide-bar macrospins cancel each other's dipolar-field, reducing net  $\mathbf{H}_{loc}$  and shifting the  $\chi$ -shaped vortex-mode intersection towards 0 mT. Vortex-mode field-gradients are highly non-linear, allowing enhanced control over mode-frequency in vortex-trained ASVI relative to conventional reconfigurable magnonic crystals and highlighting the degree of spectral-reconfigurability offered by ASVI. ASVI exhibits curved (low-frequency vortex modes), straight (macrospin modes) and flat (high-frequency vortex mode) mode gradients, an unusually rich spin-wave mode spectra for a nanopatterned reconfigurable magnonic system. Simulations show a vortex-core gyration mode<sup>29,30</sup>  $\sim 0.1 - 0.5$  GHz, which we don't observe as our FMR is limited to 2 GHz minimum frequency.

Linking the spectral response to the microstate and showing the effects of extended training, figure 2 g) shows MFM images at 3-100 training loops, with 3-30 loop states corresponding to the FMR heatmaps. The domain growth and increasing vortex population observed over 0-4 loops in fig. 1 k) continues, with defined domain patterns observed and high-purity vortex states reached by 100 loops.

Figure 3 shows MuMax3 simulations of the spatial profiles of ASVI magnon modes at  $H_{app} = +5$  mT (fig. 3a), 0 (b) and -5 (c) mT for a vertex with vortices in both wide bars. Three main modes are observed:  $M1_A$  &  $M1_B$  are bulk-like modes localised above (A) and below (B) the vortex-core.  $M1$  modes exhibit sigmoidal field gradients with opposite  $\frac{\partial f}{\partial H}$ -sign as  $H_{app}$  causes the  $M1_A$  region to grow at the expense of  $M1_B$  as field is swept negative-to-positive and the vortex-core moves along the bar length. The macrospin thin-bars exhibit a bulk-mode  $M2$  and the vortex wide-bars exhibit a higher-order mode  $M3$  with whispering-gallery like profile around the bar edge<sup>31</sup>. Figure 3 shows simulated mode field-evolution, showing good correspondence with experimental FMR minus the wide-bar macrospin mode not present in the simulated vertex. Additional higher-index modes are resolved in simulation, these are more sensitive to nanopatterning imperfection and fall below experimental signal-to-noise threshold. The range of modes and their broad set of profiles and field-gradients are a strong example of the flexibility and benefits offered by magnetic-texture based magnonics<sup>17</sup>.

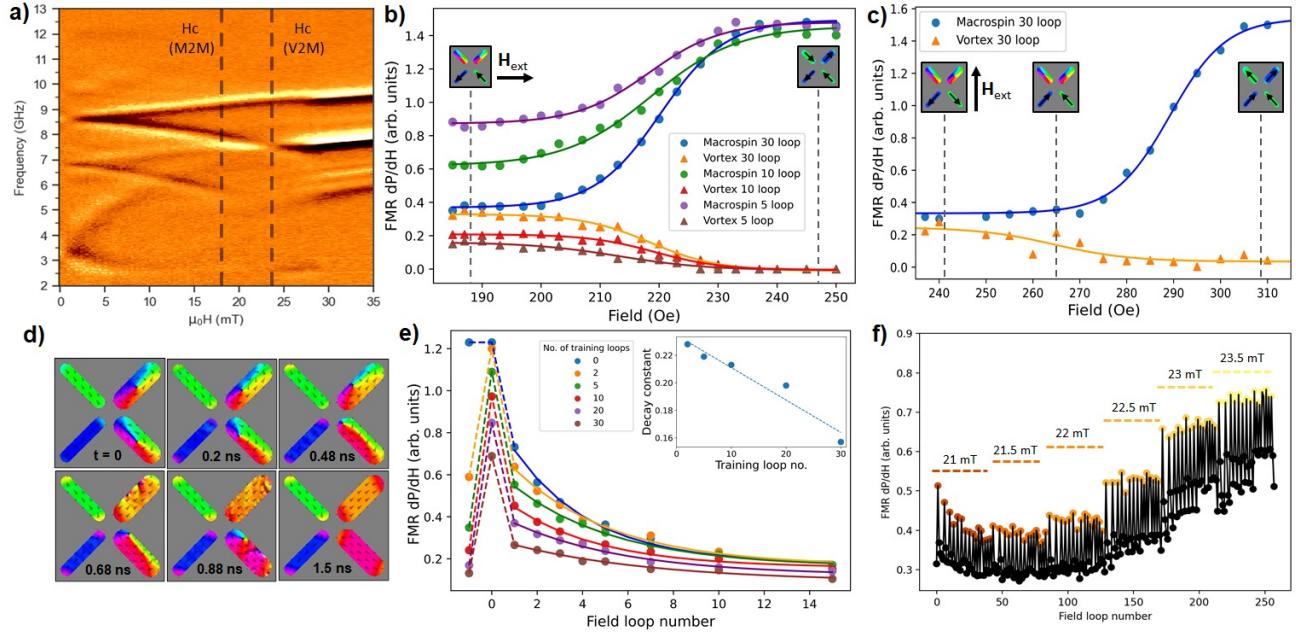


**Figure 4.** Vortex-to-macrospin conversion and complex training sequences.

- a) FMR heatmap showing 0-35 mT field sweep along  $\hat{x}$  starting from high vortex-population state, ending in saturated pure-macrospin state. Initial high-vortex population state has thin-bars and macrospin wide-bars magnetised along  $\hat{y}$ . Wide-bar macrospins switch to  $+\hat{x}$  magnetisation at 17 mT ( $H_c$  ‘M2M’), vortices switch to  $+\hat{x}$  macrospins beginning at 24 mT ( $H_c$  ‘V2M’) and saturate at 27 mT.
- b) Mode-amplitudes of wide-bar vortex and macrospin modes while positively-sweeping field from 5, 10 and  $30 \pm 18$  mT training-loop states to saturated pure-macrospin state. Spectra were measured in -1.2 mT bias field after each field application to remove effects of varying  $H_{app}$  on mode amplitudes, allowing clearer state comparison. Training-field was applied in  $\hat{x}$  direction, thin bars saturated along  $-\hat{x}$  hence V2M conversion occurs at slightly lower fields than panel (a). V2M conversion begins above 200 Oe, highlighting the ratchet effect whereby vorticisation is achieved with 18 mT training field as vortices remain stable until higher  $H_{app}$ .
- c) Mode-amplitudes of wide-bar macrospin and vortex modes while positively increasing field along  $+\hat{y}$  after  $30 \pm 19$  mT  $\hat{y}$  training loops, ending in saturated pure-macrospin state. Sample initially saturated along  $-\hat{y}$  pre-training, thin bars initially saturated along  $-\hat{y}$  before reversing at 27 mT and unlocking V2M conversion. Spectra measured in -1.2 mT bias field after each field application. V2M conversion begins at 27 mT, significantly higher than (b). This demonstrates control over protected vortex field-range via reconfigurable thin-bar bias-field.
- d) MuMax3 simulated time series of vortex-to-macrospin conversion at  $H_{app} = 21$  mT showing vortex-cores pushed by  $H_{app}$  into nanoisland edges, decomposing vortices into macrospin states.
- e) Macrospin FMR mode-amplitude response of 0, 2, 5, 10, 20 and  $30 \pm 18$  mT training loop states to a single +21.5 mT ‘stimulus’ field application, then 15 subsequent  $\pm 18$  mT ‘recovery’ training loops. 21.5 mT stimulus field is chosen following results of panel (b) to convert  $\sim 35 - 50\%$  of vortices to macrospins. Initial trained state amplitudes are shown at field loop number -1, 21.5 mT stimulus field is applied at loop 0, loops 1-15 are  $\pm 18$  mT training loops. States retain training memory (i.e. longer-trained states exhibit lower macrospin mode amplitudes) many loops after the 21.5 mT field application. Post-stimulus training rate  $\tau$  is fitted and plotted inset as a function of  $n$  (number of pre-stimulus training loops). Linear fitting gives  $\tau = -2.35 \times 10^{-3}n + 0.235$ ,  $R^2 = 0.94$ .
- f) Macrospin mode-amplitude evolution over training series consisting of single 21-23.5 mT ‘stimulus’ field applications followed by two subsequent  $\pm 18$  mT loops. Stimulus fields convert vortices to macrospins, 18 mT loops convert macrospins to vortices. Sensitive response of mode-amplitude gradient to applied-field magnitude is observed. System begins at loop 0 in a highly-vorticised state.

## Vortex to macrospin conversion

The vorticisation process is bidirectional with distinct switching dynamics and coercive fields when converting vortices to macrospins. Figure 4a) shows an FMR heatmap starting at 0 mT with a 30-loop, high vortex-population state then sweeping  $\mathbf{H}_{ext}$  0-35 mT. Macrospins in the initial state are magnetised along  $+\hat{\mathbf{y}}$ ,  $\mathbf{H}_{ext}$  swept along  $+\hat{\mathbf{x}}$ . Three switching behaviours are observed: Wide-bar macrospins switching at 15.5-17 mT, thin-bar macrospins at 27 mT, and V2M conversion from 24-28 mT. The tapering linewidth of the  $\sim 7.5$  GHz wide-bar macrospin mode between 24-28 mT reveals details of quenched-disorder effects in V2M-conversion (see supplementary note 2).

Figure 4 b) shows V2M conversion for 5, 10 and 30 training-loop states, trained at  $\pm 18$  mT along  $\hat{\mathbf{x}}$  and swept 0-25 mT along  $+\hat{\mathbf{x}}$  until reaching a saturated all-macrospin state. Phenomenological fits to macrospin and vortex mode-amplitudes are achieved using sigmoid functions. For all training states V2M conversion begins at  $\mathbf{H}_{ext} = 19.5$  mT, reaching saturated all-macrospin states at 23.8 mT. This gives a training-field window 18-19.5 mT above the wide-bar coercive field and below V2M conversion within which to exploit the vortex-training ratchet effect.

Figure 4 c) demonstrates further the reconfigurable control provided by the thin-bars. We prepare a 30-loop state trained  $\pm 19$  mT along  $\hat{\mathbf{y}}$  with  $-\hat{\mathbf{y}}$  magnetised thin bars then sweep 0-31 mT along  $+\hat{\mathbf{y}}$  until saturating into macrospin state. Here, V2M conversion is prevented until a higher field, beginning at 26.5 mT and saturating at 30.5 mT. This is due to dipolar vertex energetics. With  $\mathbf{H}_{ext}$  along  $\hat{\mathbf{y}}$  and  $-\hat{\mathbf{y}}$  saturated thin bars, vortices converting to macrospins would enter the ‘type 4’ or ‘monopole’ state<sup>4,19</sup>, highly energetically-unfavourable repulsive configurations which impede motion of vortex-cores towards bar-edges. Figure 4e) is a MuMax3 time-series showing V2M-conversion occurs by the vortex-core reaching the bar-edge before decomposing to the pair of  $+\frac{1}{2}$  edge-bound topological defects characterising the macrospin state, hence increased V2M conversion field when switching into type-4 states. At 26.5 mT thin-bars switch to  $\mathbf{M} = +\hat{\mathbf{y}}$ . Vortices converting to macrospins will now enter lower-energy ‘type 2’ states (fig. 1 c) allowing the vortex-core to migrate towards the bar-edge with dipolar attraction and V2M-conversion begins.

Figure 4d) shows a MuMax3 times series of V2M conversion at  $H_{app} = 21$  mT. Vortex-cores are pushed by  $H_{app}$  towards bar edges ( $t=0.48$  ns) where they decompose on contact ( $t=0.68-0.88$  ns) into pairs of edge-bound  $+\frac{1}{2}$ -defects characterising the macrospin state ( $t=1.5$  ns).

Partial conversion of vortex populations to macrospins can affect subsequent training behaviour. In figure 4 e) we prepare 0-30 loop states at  $\pm 18$  mT then apply a ‘stimulus’ field of  $+21.5$  mT, chosen to convert  $\sim 35 - 50\%$  of vortices to macrospins. After stimulus field application, the system is subjected to  $15 \pm 18$  mT  $\hat{\mathbf{x}}$  training loops. Wide-bar macrospin mode amplitude is measured at each step, with step number -1 the pre-stimulus trained state, step 0 the response to the stimulus field and steps 1-15 the post-stimulus training loops.

Looking at initial trained state amplitudes, as expected we observe lower macrospin amplitudes for longer training. After stimulus-field application (loop-number 0), we observe that the longer the training, the smaller the increase of macrospin mode-amplitude in response to stimulus field. This is somewhat surprising, as longer-trained states have larger vortex populations, and therefore more bars available to convert to macrospins. This shows vortex-domains collectively resist V2M conversion. This is an important finding that shows ASVI retains memory of its training over long training histories, exhibiting substantially different responses to identical stimuli based on history. We now examine response to post-stimulus  $\pm 18$  mT loops. As in fig. 2 b), we observe exponential decay of macrospin mode-amplitude. We find the training rate  $\tau$  is a function of pre-stimulus training  $\tau = -2.35 \times 10^{-3}n + 0.235$  with  $n$  the number of pre-stimulus training loops, plotted inset in fig. 4 e). This shows the underlying training dynamics are themselves history-dependent. Additionally, longer-trained states exhibit lower macrospin mode amplitudes even 15 loops after the stimulus field. This shows ASVI training history is a persistent and measurable property. One can distinguish shorter and longer trained samples even after long training sequences and stimulus-field applications.

ASVI is highly-sensitive to small changes in applied-field amplitude, leading to complex nonlinear responses to training-sequences comprising different field-amplitudes. Figure 4f) shows macrospin mode-amplitude evolution over a training-sequence comprising single 21-23.5 mT ‘stimulus’ field applications followed by two subsequent  $\pm 18$  mT loops. System begins at loop 0 in a highly-vorticised state. Stimulus fields convert vortices to macrospins, 18 mT loops convert macrospins to vortices. Stimulus-field amplitude changes of 0.5 mT are enough to modify training behaviour and mode-amplitude gradient, shown by the diverse range of amplitude gradients over the training sequence.

## Local training control via vortex writing

As mentioned throughout, training behaviour is highly-dependent on the local dipolar-field landscape. We have observed that vortices locally increase vorticisation likelihood, and macrospins may become pinned due to their surrounding dipolar-field landscape. So far these effects have been observed stochastically, spatially-dispersed throughout the array. However, we may leverage the previously described ‘Topological defect-driven Magnetic Writing’ (TMW)<sup>27</sup> to manually write vortices using an MFM tip. These locally-induced vortices dramatically alter the field-response of surrounding bars. Figure 5 a-c) show MFM images of a tip-writing process where an initial all-macrospin state (a) is modified by writing a 6-bar vortex-chain (b) then a

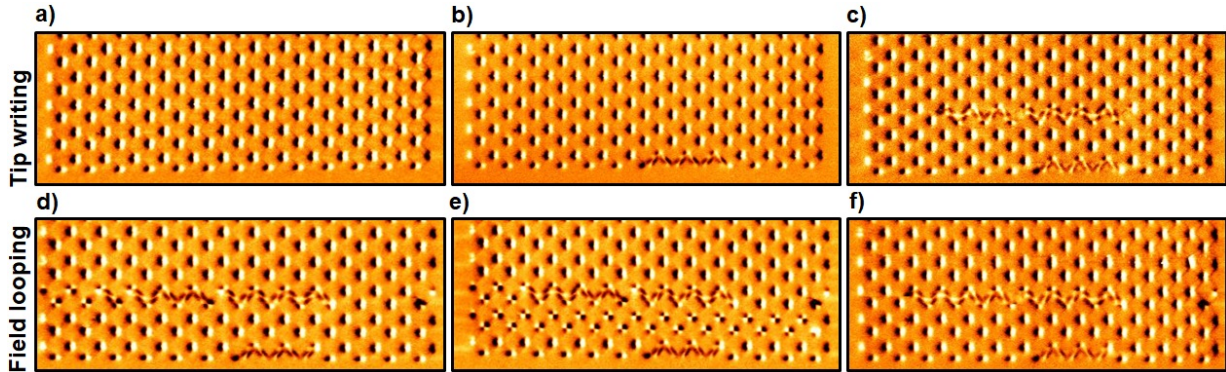


**Figure 5.** Vortex writing via MFM-tip and influence on local switching dynamics.

a-c) Tip-writing of two vortex lines. Beginning from a negatively saturated pure-macrospin state (a) we scan a high-moment MFM tip across 6 wide bars at the bottom of the array, resulting in vortication of the scanned bars (b). We then scan the tip across a line of 14 wide bars (c), resulting in vortication of all scanned bars including a double-vortex state in two bars, the right-most bar and a bar near the centre of the written line.

d-f) Field-looping of MFM tip-written vortex states. From the two-line state in panel (c), a single  $+\hat{x}$  field of 13 mT was applied (d), well below the coercive field of 18 mT for macrospin wide-bars in a typical field-saturated state. Panel (d) shows switching of bars to the left of the upper vortex line, vorticing another bar and creating a chain of ground-state vertices. A subsequent  $\pm 13$  mT loop was applied (e), resulting in the ground-state vertex chain developing into a larger domain between the two written vortex lines, demonstrating the substantial effects on local switching behaviour achieved by targeted vortex writing. A single -13 mT field was applied to return the system to the originally written two vortex-line state (f), highlighting the intrinsic memory capabilities of ASVI.

14-bar vortex-chain (c). Figure 5 d-f) show the effects of field-looping the tip-written vortex-chain state. A field of  $H_{app} = 13$  mT is used, substantially lower than the 15.5-17 mT required to reverse macrospins from a saturated state. Figure 5 d) shows the state after applying a +13 mT field. Several bars have reversed, adding another vortex to the upper chain and reversing a row of wide-bar macrospins left of the vortex-chain. Figure 5 e) shows the state after a subsequent  $\pm 13$  mT loop. An entire row of macrospins between the upper and lower vortex-chains has reversed, forming a ‘type 1’ ground-state domain while the rest of the array remains unaffected, demonstrating the degree of local training control available via vortex-writing. Figure 5 f) shows the state after applying a further single -13 mT field. This resets the type-1 macrospin domain while leaving the tip-written vortices. These results demonstrate the persistent nature of written vortices and their ability to radically alter local ASVI memory behaviour, serving as a form of targeted reconfigurable quenched disorder and substantially lowering neighbouring coercive fields.

We have demonstrated ASVI, a four-state spin-system with engineered texture bistability giving rise to emergent dynamics including collective physical memory phenomena and highly-reconfigurable spin-wave spectra. The ability of vortices to locally modify memory and switching behaviour is exciting, particularly when manually tip-written, and highlights the benefits of diverse magnetic textures in artificial spin systems. Vortex chains and domains may be harnessed to define magnon waveguides<sup>32,33</sup>, self-assembled via field-training or tip-written. The vortex-to-macrospin frequency shift of  $\Delta f = 3.8$  GHz is competitively high across reconfigurable magnonics and the analogue-style mode-amplitude tuning has technological appeal. As artificial spin systems stray further from their initial role as model thermodynamic systems their scope and utility broadens, with more complex and diverse systems offering next-generation physics and functionality sure to follow.

## Author contributions

JCG, AV and KDS conceived the work.

JCG drafted the manuscript, with contributions from all authors in editing and revision stages.

JCG, KDS and AV performed FMR measurements.

JCG and HH performed MFM measurements.

JCG and KDS fabricated the ASVI. AV performed CAD design of the structures.

AV and JCG performed MOKE measurements of coercive field.

TD wrote code for simulation of the magnon spectra and performed micromagnetic simulations of mode dispersion relations and spatial mode profiles. TD performed mode character analysis and identification.

DMA wrote code for simulation of the magnon spectra.

HK contributed analysis of spin-wave dynamics.

WRB oversaw the project and provided critical feedback and direction throughout.

## Acknowledgements

This work was supported by the Leverhulme Trust (RPG-2017-257) to WRB.

TD and AV were supported by the EPSRC Centre for Doctoral Training in Advanced Characterisation of Materials (Grant No. EP/L015277/1).

Simulations were performed on the Imperial College London Research Computing Service<sup>34</sup>.

The authors would like to thank Professor Lesley F. Cohen of Imperial College London for enlightening discussion and comments and David Mack for excellent laboratory management..

## Competing interests

The authors declare no competing interests.

## Data availability statement

The datasets generated during and/or analysed during the current study are available from the corresponding author on reasonable request.

## Code availability statement

The code used in this study is available from the corresponding author on reasonable request.

## Supplementary Information

### Methods

#### Micromagnetic simulation

Simulations were performed using MuMax3. To maintain field sweep history, ground state files are generated in a separate script and used as inputs for dynamic simulations. Material parameters for NiFe used are; saturation magnetisation,  $M_{sat} = 750 \text{ kA/m}$ , exchange stiffness,  $A_{ex} = 13 \text{ pJ}$  and damping,  $\alpha = 0.001$ . All simulations are discretised with lateral dimensions,  $c_{x,y} = 5 \text{ nm}$  and normal direction,  $c_z = 10 \text{ nm}$  and periodic boundary conditions applied to generate lattice from unit cell. A broadband field excitation sinc pulse function is applied along z-direction with cutoff frequency = 20 GHz, amplitude = 0.5 mT. Simulation is run for 25 ns saving magnetisation every 25 ps. Static relaxed magnetisation at  $t = 0$  is subtracted from all subsequent files to retain only dynamic components, which are then subject to an FFT along the time axis to generate a frequency spectra. Power spectra across the field range are collated and plotted as a colour contour plot with resolution;  $\Delta f = 40 \text{ MHz}$  and  $\Delta \mu_0 H = 1 \text{ mT}$ . Spatial power maps are generated by integrating over a range determined by the full width half maximum of peak fits and plotting each cell as a pixel whose colour corresponds to its power. Each colour plot is normalised to the cell with highest power. High-resolution simulations performed for figure 3 have lower damping,  $\alpha = 0.0001$ , and are run for 100 ns saving every 50 ps. The lower damping serves just to reduce linewidth for clarity of visualisation, and other behaviours associated with more realistic higher damping are well preserved<sup>35</sup>. This produces colour plots with resolution;  $\Delta f = 10 \text{ MHz}$  and  $\Delta \mu_0 H = 0.2 \text{ mT}$ .  $\mathbf{H}_{ext}$  is offset from the array  $\hat{x}, \hat{y}$ -axes by  $1^\circ$  to better match experiment.

#### Nanofabrication

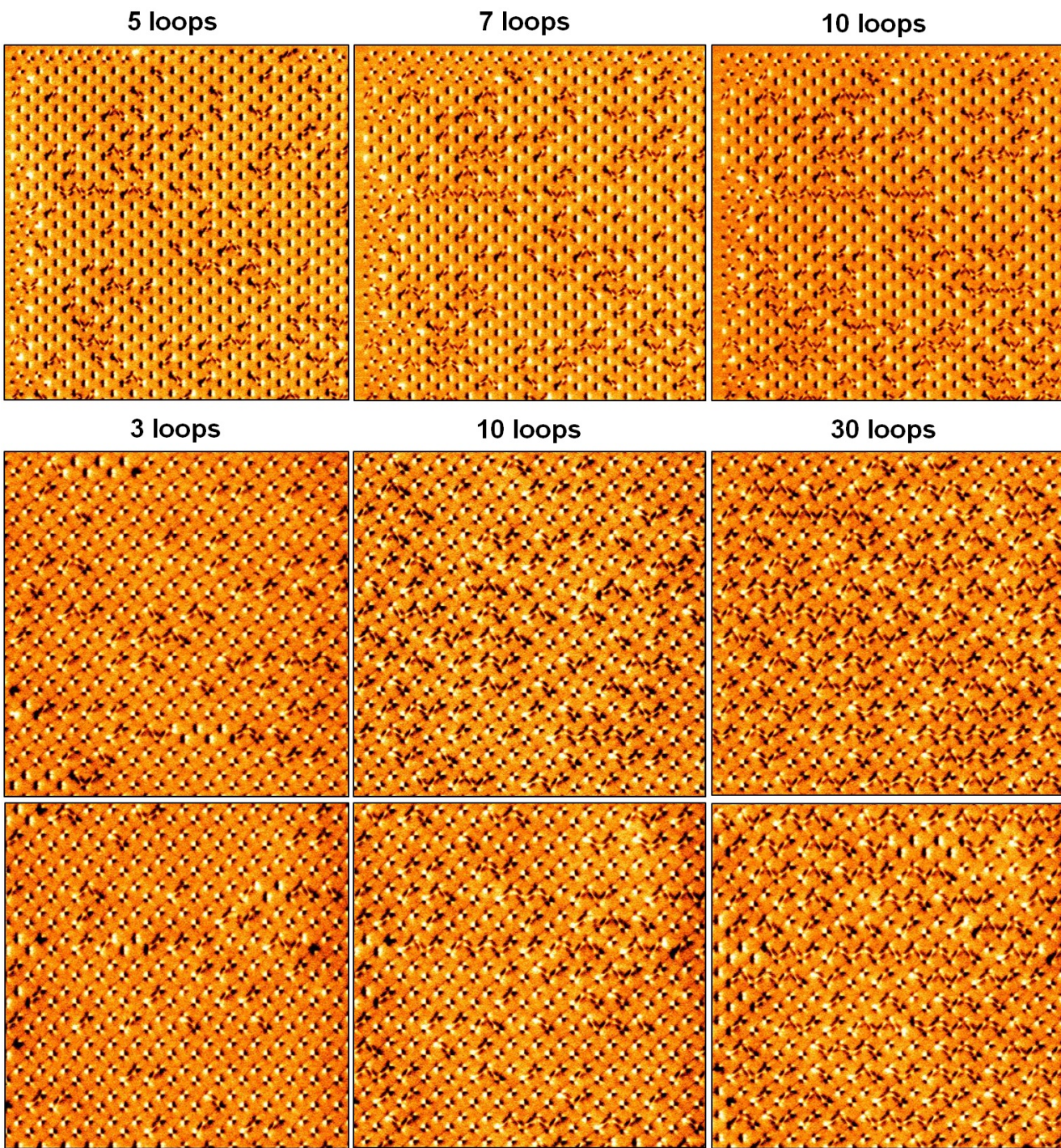
ASVI was fabricated via electron-beam lithography liftoff method on a Raith eLine system with PMMA resist. Ni<sub>81</sub>Fe<sub>19</sub> (permalloy) was thermally evaporated and capped with Al<sub>2</sub>O<sub>3</sub>. A ‘staircase’ subset of bars was increased in width to reduce its coercive field relative to the thin subset, allowing independent subset reversal via global field.

#### FMR measurement

Ferromagnetic resonance spectra were measured using a NanOsc Instruments cryoFMR in a Quantum Design Physical Properties Measurement System. Broadband FMR measurements were carried out on large area samples ( $\sim 2 \times 2 \text{ mm}^2$ ) mounted flip-chip style on a coplanar waveguide. The waveguide was connected to a microwave generator, coupling RF magnetic fields to the sample. The output from waveguide was rectified using an RF-diode detector. Measurements were done in fixed in-plane field while the RF frequency was swept in 10 MHz steps. The DC field was then modulated at 490 Hz with a 0.48 mT RMS field and the diode voltage response measured via lock-in. The experimental spectra show the derivative output of the microwave signal as a function of field and frequency. The normalised differential spectra are displayed as false-colour images with symmetric log colour scale.

#### MFM measurement

Magnetic force micrographs were produced on a Dimension 3100 using commercially available normal-moment MFM tips.



**Supplementary figure 1**

a-c) 5-10 loop training sequence continuing from the 0-4 loop sequence in figure 1 k).

d-f) 3-30 loop training sequence, imaged after positive field arm.

g-i) Subsequent 3-30 loop training sequence on the same array area as d-f), sample is reset to all-macrospin state with 200 mT field after sequence d-f). Different vortex locations and domain patterns are observed, highlighting the stochastic rather than deterministic nature of vortex training.

## **Supplementary note 1 - Extended 5-10 loop training sequence and distinct domain structures of distinct training sequences**

Supplementary figure 1 a-c) follow on from fig. 1 k), showing progressively higher vortex population as training progresses and more defined distinct vortex and macrospin domains, along with ‘trapped’ macrospins along the top and left edges which remain pinned and do not reverse with each loop.

Supplementary figure 1 d-f) and g-i) show two separate 3-30 loop training sequences on the same array area, with the sample reset (saturated to an all-macrospin state) between the two sequences. Locations of vortex bars and the spatial domain patterns are different in each training sequence, demonstrating that vortex training is stochastically-dominated, rather than a repeating process with the same bars vorticising every time determined by quenched disorder.

## **Supplementary note 2 - Quenched disorder influence on vortex-to-macrospin conversion and spin-wave mode linewidth and frequency**

Interesting details of V2M switching are observed by following the central frequency of the wide-bar macrospin mode (border between light and dark bands) as switching progresses from 24–28 mT. If we extend the Kittel mode gradient of the saturated wide-bar macrospin mode back from its linear region 28–35 mT, the central mode frequency diverges from this gradient between 24–28 mT. Measured mode frequency is higher than the expected Kittel gradient at 24 mT, and gradually decreases while linewidth increases until it meets the Kittel gradient at 28 mT. This is due to the Gaussian distribution of bar widths and corresponding resonant frequency spread caused by quenched disorder. While wider macrospin bars with lower resonant frequency tend to reverse at lower field<sup>18</sup>, here we are switching from vortex to macrospin states rather than between oppositely-magnetised macrospins. Figure 1 b) shows thinner bars energetically favour macrospin states, and as such switch to macrospins at lower field than broader bars. Thinner bars also exhibit higher-frequency resonances, so as V2M conversion progresses the macrospin population is initially dominated by thinner, higher-frequency bars and as such shifts the central mode-frequency above the expected average resonant Kittel frequency.

## **References**

1. S. H. Skjærvø, C. H. Marrows, R. L. Stamps, L. J. Heyderman, *Nature Reviews Physics* **2**, 13 (2020).
2. . R. Wang, *et al.*, *Nature* **439**, 303 (2006).
3. T. Shinjo, T. Okuno, R. Hassdorf, K. Shigeto, T. Ono, *Science* **289**, 930 (2000).
4. S. Ladak, D. Read, G. Perkins, L. Cohen, W. Branford, *Nature Physics* **6**, 359 (2010).
5. J. P. Morgan, A. Stein, S. Langridge, C. H. Marrows, *Nature Physics* **7**, 75 (2011).
6. J. Sklenar, *et al.*, *Nature Physics* **15**, 191 (2019).
7. D. Louis, *et al.*, *Nature materials* **17**, 1076 (2018).
8. D. Grundler, *Nature Physics* **11**, 438 (2015).
9. A. Chumak, A. Serga, B. Hillebrands, *Journal of Physics D: Applied Physics* **50**, 244001 (2017).
10. A. Barman, S. Mondal, S. Sahoo, A. De, *Journal of Applied Physics* **128**, 170901 (2020).
11. M. T. Kaffash, S. Lendinez, M. B. Jungfleisch, *Physics Letters A* **402**, 127364 (2021).
12. N. C. Keim, J. D. Paulsen, Z. Zeravcic, S. Sastry, S. R. Nagel, *Reviews of Modern Physics* **91**, 035002 (2019).
13. G. Tanaka, *et al.*, *Neural Networks* **115**, 100 (2019).
14. K. Nakajima, *Japanese Journal of Applied Physics* **59**, 060501 (2020).
15. D. Marković, A. Mizrahi, D. Querlioz, J. Grollier, *Nature Reviews Physics* **2**, 499 (2020).
16. A. Aqeel, *et al.*, *Physical Review Letters* **126**, 017202 (2021).
17. H. Yu, J. Xiao, H. Schultheiss, *Physics Reports* (2021).
18. A. Vanstone, *et al.*, *arXiv preprint arXiv:2106.04406* (2021).
19. J. C. Gartside, *et al.*, *Nature Communications* **12**, 1 (2021).
20. K. L. Metlov, K. Y. Guslienko, *Journal of magnetism and magnetic materials* **242**, 1015 (2002).
21. K. Y. Guslienko, *Journal of nanoscience and nanotechnology* **8**, 2745 (2008).
22. A. Talapatra, N. Singh, A. Adeyeye, *Physical Review Applied* **13**, 014034 (2020).
23. J. Gartside, D. Burn, L. Cohen, W. Branford, *Scientific reports* **6**, 32864 (2016).

24. C. Nisoli, *et al.*, *Physical review letters* **98**, 217203 (2007).
25. G. Möller, R. Moessner, *Physical Review B* **80**, 140409 (2009).
26. C. Kittel, *Physical review* **73**, 155 (1948).
27. J. C. Gartside, *et al.*, *Nature nanotechnology* **13**, 53 (2018).
28. Y.-L. Wang, *et al.*, *Science* **352**, 962 (2016).
29. K. Chou, *et al.*, *Applied Physics Letters* **90**, 202505 (2007).
30. A. Barman, S. Barman, T. Kimura, Y. Fukuma, Y. Otani, *Journal of Physics D: Applied Physics* **43**, 422001 (2010).
31. K. Schultheiss, *et al.*, *Physical review letters* **122**, 097202 (2019).
32. K. D. Stenning, *et al.*, *ACS nano* (2020).
33. A. Papp, W. Porod, G. Csaba, *arXiv preprint arXiv:2012.04594* (2020).
34. Imperial college research computing service. DOI: 10.14469/hpc/2232.
35. D. D. Stancil, A. Prabhakar, *Spin waves*, vol. 5 (Springer, 2009).